PERGAMON

International Journal of Solids and Structures 36 (1999) 4841–4868

INTERNATIONAL JOURNAL OF SOLIDS and STRUCTURES

Coupled fields in a deformable unsaturated medium

Y. Zhou, R. K. N. D. Rajapakse*, J. Graham

Department of Civil and Geological Engineering, University of Manitoba, Winnipeg, Canada R3T 5V6

Received 20 August 1997; accepted 29 March 1998

Abstract

This paper considers several problems involving coupled heat–moisture–air flow in deformable unsaturated media. A set of coupled non-linear governing equations expressed in terms of displacements, capillary pressure, air pressure and temperature are used in the analysis. The mathematical model accounts for fully coupled heat and moisture flow, volume strain effects on water-air-heat flow, stress and temperature dependence of the water retention curve, heat sink due to thermal expansion, phase change between liquid water and vapour water, and compressibility of liquid water. Numerical solutions are obtained by using the finite element method. Comparisons with existing analytical and experimental results for problems involving infiltration, drying–rewetting (hysteresis effects) and heating confirm the general validity of the present mathematical model. Coupled fields in a confined clay cylinder are also examined. It is found that consideration of absorbed liquid flow due to thermal gradients (thermo-osmosis effect) results in increased drying and shrinkage near the heated boundary. The case of a confined clay cylinder under combined heating and infiltration is also studied. Important features of coupled fields are discussed. © 1999 Elsevier Science Ltd. All rights reserved.

1. Introduction

An unsaturated soil is a multi-phase system that consists of a solid skeleton (soil grains) and voids containing air, water vapour and liquid water. The response of an unsaturated medium to mechanical, thermal and hydraulic loading is complex. Significant couplings exist between deformations, heat flow and moisture flow. The non-linear nature of constitutive properties makes it difficult to establish fully coupled mathematical models. Past studies were therefore based on many assumptions. A commonly used assumption is the complete rigidity of the medium ignoring the effects of deformations. Models based on this assumption are often used in soil science, water resources, engineering and agricultural engineering to study coupled heat–moisture flow in unsaturated soils. Philip and de Vries (1957) pioneered the modeling of rigid unsaturated media under gradients of temperature and moisture content. A modified version of Philip–de Vries model

---

* Corresponding author. Fax: 001 204 474 7513; E-mail: rajapal@cc.umanitoba.ca

PII: S0020-7683(98)00268-6

was proposed by Milly (1982) by using water potential and temperature as the basic variables instead of moisture content and temperature. Many extensions and applications of Philip–de Vries type models are reported in the literature over the past forty years.

The study of deformable unsaturated media is gaining attention recently due to applications in geoenvironmental engineering, geothermal energy extraction, petroleum engineering, etc. Several recent studies (McTigue, 1990; Rehbinder, 1995 and others) considered the problem of a heated cylindrical borehole in a saturated medium. These studies are based on classical Biot type models (Biot, 1956) and provided some insight into basic features of coupled fields due to heating of a saturated medium. However, the above studies are of limited use in understanding the heat induced coupled fields in an unsaturated medium. This is due to fundamental differences in the physics of saturated and unsaturated media.

The development of mathematical models for hygro-thermo-mechanics of unsaturated media requires establishment of a set of constitutive relations and balance equations. Matyas and Radhakrishna (1968), Fredlund and Hasan (1979), Lloret and Alonso (1980) and Wheeler and Sivakumar (1995) presented constitutive relations for isothermal conditions. The development of nonlinear constitutive relations for hygro-thermo-mechanical response of unsaturated soils is still in its infancy. Recent experimental studies (Graham et al., 1996) presented some preliminary framework for nonisothermal constitutive modeling and confirmed the dependence of the water retention curve (or soil water characteristic curve) on temperature and stress. Thomas and He (1995), and Thomas et al. (1996) presented mathematical models to describe the coupled heat–moisture–air flow in an unsaturated medium. These models were based on Darcy's law for air and pore water transfer and Philip-de Vries model for vapour transfer.

Recently, Zhou et al. (1998) proposed a new hygro-thermo-mechanical model which takes into account the absorbed liquid flow due to temperature gradient (thermo-osmosis), advection of heat of wetting due to water potential gradient (thermal-filtration), volume strain effects on heat–moisture–air flow, convective heat flow, temperature and stress effects on the water retention curve, temperature effects on void ratio, heat of wetting, heat sink due to thermal deformation, and compressibility of constituents. The objective of this study is to use the mathematical model of Zhou et al. (1998) to study several practically useful problems involving infiltration, drying-rewetting (hysteresis included), heating, and combined heating and infiltration of unsaturated deformable media. Comparisons are presented with Philip's (1957) quasi-analytical solution for isothermal infiltration, and experimental studies of Gillham et al. (1979) and Villar et al. (1993).

2. Hygro-thermo-mechanical model

Consider a homogeneous and statistically isotropic porous medium subjected to small deformations and infinitesimal strains. Displacements (u_i), capillary pressure (p_c), air pressure (p_a) and temperature increase (T) are chosen as the basic variables in the formulation. The stress state of an unsaturated medium can be defined in terms of ($\sigma_{ij}+\delta_{ij}p_a$) and p_c ($=p_l-p_a$) where p_l denotes the pore water pressure and σ_{ij} denote total stress positive for tension. The following section summarizes the model proposed by Zhou et al. (1998).

The equilibrium equation of the medium is given by

$$\sigma_{ij,j}+b_i = 0 \tag{1}$$

where b_i denotes the body force in the i-direction.

The following linear constitutive relationship can be postulated in the absence of validated non-linear models.

$$\sigma_{ij} = 2G\left(\varepsilon_{ij}+\delta_{ij}\frac{v}{1-2v}\varepsilon_{kk}\right)-KB_1\delta_{ij}p_c-\delta_{ij}p_a-K\alpha\delta_{ij}T \tag{2}$$

where ε_{ij} denotes the strain tensor; G is the shear modulus; v is the Poisson's ratio; K $(=2G(1+v)/3(1-2v))$ is the bulk modulus of the medium; B_1 is the coefficient of compressibility of the soil medium with respect to a change in capillary pressure; and α is the volumetric thermal expansion coefficient.

The mass balance equation of liquid water in a deformable porous medium can be expressed as

$$\frac{\partial[\rho_1(1+e)\theta]}{(1+e)\partial t} = -\nabla(q_{\text{liq}})-E \tag{3}$$

where ρ_1 is the density of liquid water, e is the void ratio, θ is the volumetric water content, q_{liq} is the liquid water flux per unit area (kg s^{-1} m^{-2}), E is the rate of water evaporation accounting for the transfer of moisture between the liquid and vapour phases and t denotes time.

In order to express the water mass balance equation in terms of basic variables, it is necessary to define a relationship of the following form between volumetric water content, net mean stress, capillary pressure and temperature increase.

$$\mathrm{d}\theta = B_2\,\mathrm{d}\sigma+B_3\,\mathrm{d}p_c+B_4\,\mathrm{d}T \tag{4}$$

where σ $(=(\sigma_1+\sigma_2+\sigma_3)/3+p_a)$ is net mean stress, B_2, B_3 and B_4 are coefficients of water content changes due to changes in the net mean stress, capillary pressure and temperature respectively. Equation (4) is a modified version of the classical water characteristic curve to account for stress and temperature effects.

The liquid water flux in eqn (3) may be written as (Kay and Groenvent, 1974; Milly, 1982)

$$q_{\text{liq}} = \rho_1K_1\nabla(p_c+p_a+\rho_1gz)-\rho_1D_T\nabla T \tag{5}$$

where K_1 is the hydraulic conductivity of liquid water that depends significantly on the void ratio and water content; D_T is a phenomenological coefficient relating absorbed liquid flow due to temperature gradient (Milly, 1982); g is the gravitational acceleration and z is the vertical coordinate (positive upward).

The term involving the temperature gradient in eqn (5) does not appear in the Philip–de Vries model. Ten Berge and Bolt (1988) presented a comprehensive discussion on coupling between liquid and fluid flow in porous media, and presented both the physical and mathematical basis for the presence of a temperature gradient in the liquid water flux law. Milly (1988) also discussed the coupled flow in porous media and emphasised the inadequacy of Darcy–Buckingham flux law and the need to consider flux laws that explicitly incorporate the thermal driving force.

The mass balance equation of water in the vapour phase can be expressed as

$$\frac{\partial\{\rho_v[e-(1+e)\theta]\}}{(1+e)\partial t} = -\nabla q_{vap}+E \tag{6}$$

where ρ_v is the density of water vapour (Philip and de Vries 1957).

The vapour flux, q_{vap}, in eqn (6) is due to vapour diffusion and convection. Therefore,

$$q_{vap} = -D^*\nabla\rho_v+\rho_v v_a \tag{7}$$

where v_a is the velocity of air phase. D^* is the effective molecular diffusivity of vapour in air (Philip and de Vries, 1957).

The velocity of air phase can be calculated by Darcy's law as

$$v_a = -K_a\nabla p_a \tag{8}$$

where K_a is the conductivity of air phase and the gravitational contribution is neglected.

The mass balance equation of dry air can be written as

$$\frac{\partial\{\rho_{da}[e-(1-H)(1+e)\theta]\}}{(1+e)\partial t} = -\nabla q_{da} \tag{9}$$

where ρ_{da} is the density of dry air; H is the coefficient of solubility defined by Henry's law and q_{da} is the dry air flux per unit area.

The heat energy balance can be expressed in terms of the following single equation by assuming that the constituents of the mixture are in thermal equilibrium.

$$\frac{\partial\Phi}{(1+e)\partial t}-(T+T_0)K\alpha\frac{\partial\varepsilon_v}{\partial t} = -\nabla q_T \tag{10}$$

where Φ is the heat content, T_0 is reference absolute temperature (K) and q_T is the heat flux. The second term in eqn (10) represents heat sink due to thermal expansion of the medium.

The heat content Φ and the total heat flux q_T accounting for convection, latent heat transfer, heat conduction, and the exothermic process of wetting of the porous medium are given by

$$\Phi = \{\rho_s C_s+\rho_l(1+e)\theta C_l+\rho_v[e-(1+e)\theta]C_v+\rho_{da}[e-(1-H)(1+e)\theta]C_{da}\}T + L_0\rho_v[e-(1+e)\theta]+\rho_l(1+e)\theta W \tag{11}$$

$$q_T = q_{liq}C_lT+q_{vap}C_vT+q_{da}C_{da}T+L_0q_{vap}-\lambda\nabla T-D_c\nabla(p_c+p_a+\rho_lgz) \tag{12}$$

where C_l, C_v, C_{da}, C_s are the specific heats of liquid water, water vapour, dry air and soil grain respectively; λ is the thermal conductivity of the unsaturated medium; ρ_s is the density of soil grain; L_0 is latent heat of evaporation at reference temperature (T_0); D_c [$=(T+T_0)D_T$] is the thermal-filtration coefficient accounting for advection of heat of wetting due to liquid potential gradient (Kay and Groenvelt, 1974; Milly, 1982), W is the differential heat of wetting (J kg^{-1}) (Milly, 1984).

The manipulation of balance equations and substitution of additional basic relationships (Zhou et al., 1998) results in the following governing equation system expressed in terms of the basic unknowns displacements (u_i), capillary pressure (p_c), air pressure (p_a) and temperature (T).

$$\nabla^2u_i+\frac{G}{1-2v}u_{j,ji}-p_{a,i}-KB_1p_{c,i}-K\alpha T_{,i}+b_i = 0 \tag{13}$$

$$(L_{11}+L_{21})\frac{\partial \varepsilon_{\mathrm{v}}}{\partial t}+(L_{12}+L_{22})\frac{\partial p_{\mathrm{c}}}{\partial t}+(L_{13}+L_{23})\frac{\partial p_{\mathrm{a}}}{\partial t}+(L_{14}+L_{24})\frac{\partial T}{\partial t}$$
$$=\nabla[(\rho_{\mathrm{l}}K_{\mathrm{l}}+D_{1}^{*})\nabla p_{\mathrm{c}}\}+\nabla[(\rho_{\mathrm{v}}K_{\mathrm{a}}+\rho_{\mathrm{l}}K_{\mathrm{l}}+D_{2}^{*})\nabla p_{\mathrm{a}}]+\nabla[(\rho_{\mathrm{l}}D_{T}+D_{3}^{*})\nabla T\}$$
$$+\nabla[(\rho_{\mathrm{l}}K_{\mathrm{l}}\nabla(\rho_{\mathrm{l}}gz)] \tag{14}$$

$$L_{31}\frac{\partial \varepsilon_{\mathrm{v}}}{\partial t}+L_{32}\frac{\partial p_{\mathrm{c}}}{\partial t}+L_{33}\frac{\partial p_{\mathrm{a}}}{\partial t}+L_{34}\frac{\partial T}{\partial t}=\nabla(H\rho_{\mathrm{da}}K_{\mathrm{l}}\nabla p_{\mathrm{c}})$$
$$+\nabla[\rho_{\mathrm{da}}(K_{\mathrm{a}}+HK_{\mathrm{l}})\nabla p_{\mathrm{a}}]+\nabla(H\rho_{\mathrm{da}}D_{T}\nabla T)+\nabla[H\rho_{\mathrm{da}}K_{\mathrm{l}}\nabla(\rho_{\mathrm{l}}gz)] \tag{15}$$

$$L_{41}\frac{\partial \varepsilon_{\mathrm{v}}}{\partial t}+L_{42}\frac{\partial p_{\mathrm{c}}}{\partial t}+L_{43}\frac{\partial p_{\mathrm{a}}}{\partial t}+L_{44}\frac{\partial T}{\partial t}$$
$$=\nabla[D_{\mathrm{c2}}^{*}\nabla p_{\mathrm{c}}+D_{\mathrm{a2}}^{*}\nabla p_{\mathrm{a}}+D_{T2}^{*}\nabla T+(D_{\mathrm{c}}+(C_{\mathrm{l}}\rho_{\mathrm{l}}+C_{\mathrm{da}}\rho_{\mathrm{da}}H)K_{\mathrm{l}}T)\nabla(\rho_{\mathrm{l}}gz)] \tag{16}$$

where the coefficients L_{ij} ($i = 1, 3; j = 1, 4$), D_{a2}^{*}, D_{c2}^{*}, D_{T2}^{*}, D_{k}^{*} ($k = 1, 3$) are defined in Appendix 1.

3. Finite element scheme

The mathematical model presented in the preceding section has to be solved numerically. The Galerkin method (Zienkiewicz and Taylor, 1989) is introduced to obtain a finite element representation of eqns (13)–(16). The basic variables displacements, capillary pressure, air pressure and temperature are interpolated as,

$$\mathbf{u}(t) = \mathbf{N}\hat{\mathbf{U}}(t); \quad \mathbf{p}_{\mathrm{c}}(t) = \mathbf{N}\hat{\mathbf{p}}(t); \quad \mathbf{p}_{\mathrm{a}}(t) = \mathbf{N}\hat{\mathbf{p}}_{\mathrm{a}}(t); \quad \mathbf{T}(t) = \mathbf{N}\hat{\mathbf{T}}(t) \tag{17}$$

where $\hat{\mathbf{U}}(t)$, $\hat{\mathbf{P}}_{\mathrm{c}}(t)$, $\hat{\mathbf{P}}_{\mathrm{a}}(t)$, and $\hat{\mathbf{T}}(t)$ are vectors of nodal displacements, capillary pressure and temperature at time t; and $\mathbf{N}$ is a shape function matrix. In Zhou et al. (1998), a mixed type Galerkin formulation of the governing equations that also interpolates porosity of the medium in addition to the basic variables was used to study one-dimensional soil column problems. In this paper the mixed formulation is not used to test the accuracy and numerical stability of the standard Galerkin formulation for the present class of problems.

The application of finite element procedures to eqns (13)–(16) with $\mathbf{N}$ as the weight function (Zienkiewicz and Taylor, 1989) results in

$$\mathbf{G}\dot{\mathbf{X}}+\mathbf{K}\mathbf{X} = \mathbf{F} \tag{18}$$

The coefficient matrices $\mathbf{G}$ and $\mathbf{K}$ depend on the nodal unknowns. The matrices $\mathbf{G}$ and $\mathbf{K}$ and vectors $\mathbf{X}$ and $\mathbf{F}$ in eqn (18) are given in Appendix 2. There are many methods for solving non-linear equations of this type (Zienkiewicz and Taylor, 1989). In the present study, a backward difference time-stepping scheme is adopted because of several computational advantages (Lewis and Schrefler, 1987). A finite element code based on the above formulation has been developed to analyze radially symmetric and axially symmetric problems using two node linear and three node axisymmetric triangular elements respectively. Each node in the axisymmetric case has five unknowns (displacements in the r- and z-directions, capillary pressure, air pressure and temperature). The **G** matrix in eqn (19) is diagonalized by adding all the non-diagonal elements to the diagonal element to achieve stable numerical solutions (Zienkiewicz and Taylor, 1989).

4. Results and discussion

A computer program based on the above finite element formulation has been developed. The validation of a mathematical model for the present class of problems is a difficult and complex task due to various coupling processes, the large number of constitutive properties involved and related nonlinearities. Analytical solutions for simplified cases and extensive experimental work are needed in order to establish the accuracy of the finite element algorithm and the overall applicability of the present mathematical model for engineering applications. Since there are many coupled processes involved, it is useful to investigate uncoupled systems initially and then move on to the simulation of fully coupled effects. Five problems are considered in this section. In the first three examples, the finite element solutions are compared with an analytical solution for a simplified infiltration problem and experimental studies involving drying-rewetting and heating of soils to test the general validity of the model. Thereafter, the computer code is used to simulate problems involving heating and combined heating-infiltration of an annular clay cylinder.

4.1. Case 1

The first problem considered is infiltration into unsaturated Yolo light clay for which Philip (1957) developed a quasi-analytical solution for a semi-infinite medium. In the current analysis, the effects of deformation, air and vapour transfer, temperature and coupled heat and fluid flow are all neglected. The governing equation is thus eqn (14) with ρ_v set equal to zero and T held constant, i.e.,

$$\frac{\mathrm{d}\theta}{\mathrm{d}\psi}\frac{\mathrm{d}\psi}{\mathrm{d}t} = \frac{\partial}{\partial z}\left[K_l\left(\frac{\partial\psi}{\partial z}+1\right)\right] \tag{19}$$

where $\psi\ [=p_c/(\rho_l g)]$ is water pressure head.

This is the same nonlinear partial differential equation studied by Philip (1957).

In the finite element analysis, a 40 cm long clay column is considered with the following boundary and initial conditions:

$$\begin{aligned}&\psi = -600\,\text{cm}; \quad t = 0 \quad -40\,\text{cm} \leqslant z \leqslant 0\,\text{cm}\\ &\psi = 0\,\text{cm}; \quad t > 0 \quad z = 0\,\text{cm}\\ &\psi = -600\,\text{cm}; \quad t > 0 \quad z = -40\,\text{cm}\end{aligned} \tag{20}$$

Although Philip's quasi-analytical solution is for a semiinfinite medium, it can be used for solutions at early times when the wetting front is considerably away from the lower boundary of the soil column.

The hydraulic conductivity is given by Haverkamp et al. (1977) as,

$$K_l = K_{sat}/[1+(|\psi|)^{1.77}/124.6] \tag{21}$$

where $K_{\text{sat}} = 1.23 \times 10^{-5}$ cm s^{-1}, and the relationship between water content and pressure head is given by

$$\theta = 0.371\left[1+\left(\frac{\log(-\psi)}{2.26}\right)^4\right]^{-1}+0.124 \quad \psi < -1\,\text{cm}$$

$$\theta = 0.495 \quad \psi \geqslant -1\,\text{cm} \tag{22}$$

Philip's solution has often been used to test the accuracy of numerical model for unsaturated flow. Several past studies, such as Haverkamp et al. (1977), Milly (1982) and others, have compared their results with Philip's solutions. Figure 1 shows a comparison of present solutions for water content along the column with the results given by Philip (1957). The agreement is very good over a longer span of time. The results shown in Fig. 1 are based on 50 1D, 3-node elements with a surface element 0.32 cm long and the element size uniformly increased with depth. The initial time step was 10 s, and after 500 s the time step was increased to 100 s. Iterations were performed within

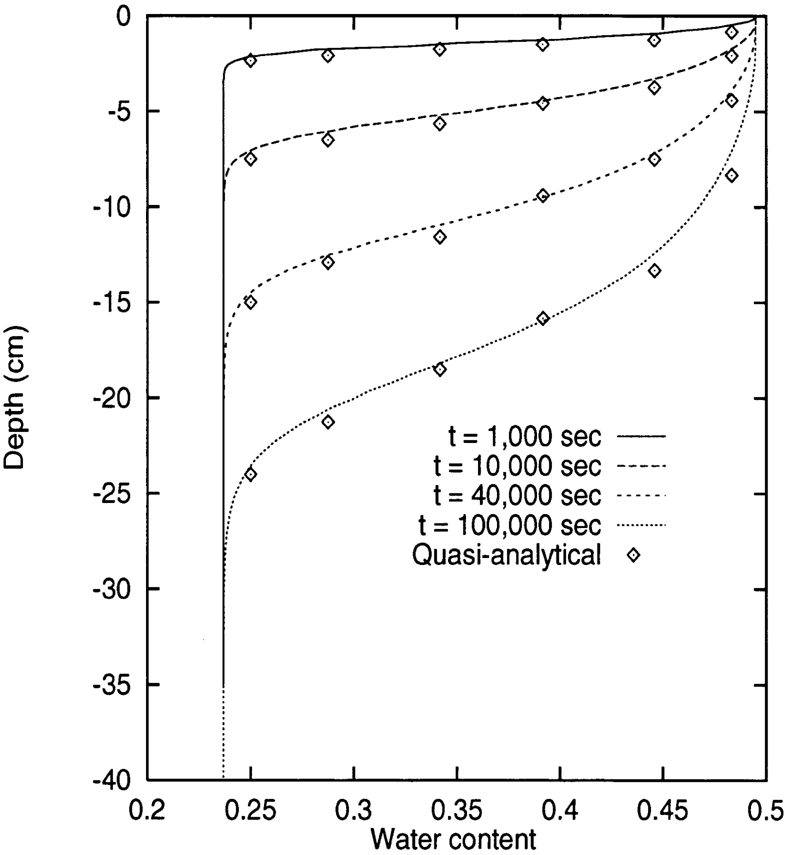

Fig. 1. Isothermal infiltration into Yolo light clay.

each time step until $|\psi_{s+1}^{k} - \psi_{s}^{k}| < \varepsilon = 10^{-5}$ at all nodes to ensure convergency, where k denotes the time step, s is iteration number and ε the convergence criterion respectively.

4.2. *Case* 2

The relationship between capillary pressure and water content (the soil water characteristic curve) is not unique and single-valued for almost all soils. The water characteristic curve can be obtained in two ways: (1) in desorption, by taking an initially-saturated sample and applying increasing suction to gradually dry the soil while taking successive measurements of water content versus capillary pressure and (2) in sorption, by gradually wetting up an initially dry soil sample while reducing the suction. The curves obtained from desorption and absorption are not identical for most soils. The equilibrium soil water content at a given capillary pressure is greater in desorption (drying) than in sorption (wetting). This dependence of the equilibrium water content and state of soil water upon the direction of the process leading up to it is called hysteresis (Hillel, 1971).

Hysteresis in soil hydraulic properties is a well recognized phenomenon but often neglected in analyses of water movement in the unsaturated zone. This may be justifiable in the case of processes involving monotonic wetting (e.g. infiltration) or drying (e.g. evaporation). But the hysteresis effect is important in the case of composite processes in which wetting and drying occur simultaneously or sequentially in various parts of the soil profile (e.g. redistribution).

As described by Hillel (1971), the hysteresis effect may be attributed to several causes: (1) the geometric nonuniformity of the individual pores in the medium which results in the 'inkbottle' effect. (2) The contact-angle between an air–water interface and a solid surface exhibits hysteresis. The angle reaches its maximum value when water moves toward a dry surface and takes its minimum value when water recedes. Given water content will tend therefore to exhibit greater suction in desorption than in sorption. (3) Different adsorbed water layers on clay surfaces due to vapour pressure change (adsorption hysteresis). (4) Entrapped air, which further decreases the water content of newly wetted soil. Failure to attain true equilibrium can accentuate the hysteresis effect. (5) Swelling, shrinking, or aging phenomena, which results in different changes of soil structure, depending on the wetting and drying history of the sample. The gradual solution of air, or the release of dissolved air from soil water, can also have a differential effect upon the water content-capillary pressure relationship in wetting and drying systems.

The two complete water characteristic curves, from saturation to dryness and vice versa, are called main branches of hysteresis—main drying curve (MDC, Fig. 2 curve A) and main wetting curve (MWC, Fig. 2 curve B), respectively. A characteristic beginning at an intermediate point on the main wetting curve and carried to maximum suction is called a primary drying scanning curve (Fig. 2, curve C), while a similar characteristic from an intermediate point on the main drying curve and carried to saturation at vanishing suction is called primary wetting scanning curve (Fig. 2, curve D). A characteristic beginning at an intermediate point on a primary curve is called a (secondary) scanning curve.

To demonstrate the applicability of the present model for situations involving hysteresis in hydraulic properties, the slow drainage–rewetting experiment described by Gillham et al. (1979) was simulated. This is a good example of hysteretic phenomena and has been modeled by several researchers, such as Pickens and Gillham (1980), Kool and Parker (1987) and others.

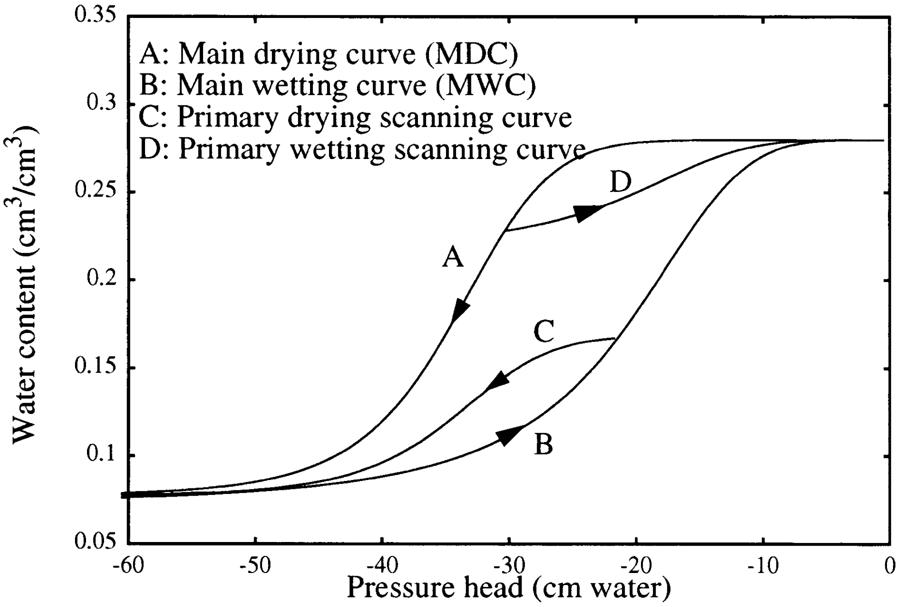

Fig. 2. Water content—pressure head hysteresis loop.

The experiment involved a 60 cm high dune sand column that was initially saturated, then allowed to drain and rewet by slowly controlling the water pressure at the bottom. The water content distribution along the column was measured at five different times ($t = 0$, 45, 68, 90 and 125 min). Kool and Parker (1987) described the main drying and wetting curve for dune sand including entrapped air effects by the following expressions.

$$\begin{aligned}
&\theta^{\mathrm{d}}(\psi) = \theta^{\mathrm{d}}_{\mathrm{r}} + (\theta^{\mathrm{d}}_{\mathrm{s}} - \theta^{\mathrm{d}}_{\mathrm{r}})\,[1 + |\alpha^{\mathrm{d}}\psi|^{n^{\mathrm{d}}}]^{-m} \quad \psi < 0\\
&\theta^{\mathrm{d}}(\psi) = \theta^{\mathrm{d}}_{\mathrm{s}} \quad \psi \geqslant 0\\
&\theta^{\mathrm{w}}(\psi) = \theta^{\mathrm{w}}_{\mathrm{r}} + (\theta^{\mathrm{w}}_{\mathrm{s}} - \theta^{\mathrm{w}}_{\mathrm{r}})\,[1 + |\alpha^{\mathrm{w}}\psi|^{n^{\mathrm{w}}}]^{-m} \quad \psi < 0\\
&\theta^{\mathrm{w}}(\psi) = \theta^{\mathrm{w}}_{\mathrm{s}} \quad \psi \geqslant 0
\end{aligned} \tag{23}$$

where $\theta^{\mathrm{d}}_{\mathrm{r}} = 0.098$, $\theta^{\mathrm{w}}_{\mathrm{r}} = 0.093$, $\theta^{\mathrm{d}}_{\mathrm{s}} = \theta^{\mathrm{w}}_{\mathrm{s}} = 0.301$, $\alpha^{\mathrm{d}} = 3.02$, $\alpha^{\mathrm{w}} = 5.47$, $n^{\mathrm{d}} = 8.904$ and $n^{\mathrm{w}} = 4.264$.

Following Kool and Parker (1987), drying scanning curves and wetting scanning curves can be derived from the main drying curve and main wetting curve, respectively, by using the model developed by Scott et al. (1983). Figure 2 shows the main drying curve (MDC), main wetting curve (MWC), primary wetting scanning curve and primary drying scanning curve of the dune sand material used in the experiment.

The soil column used in the experiment is non-homogeneous and the hydraulic parameters depend on the elevation. Gillham et al. (1979) considered an equivalent homogeneous column by using average hydraulic properties for numerical modeling purpose. Figure 3 shows the hydraulic conductivity–water content relationship which is given by (Gillham et al., 1979) as

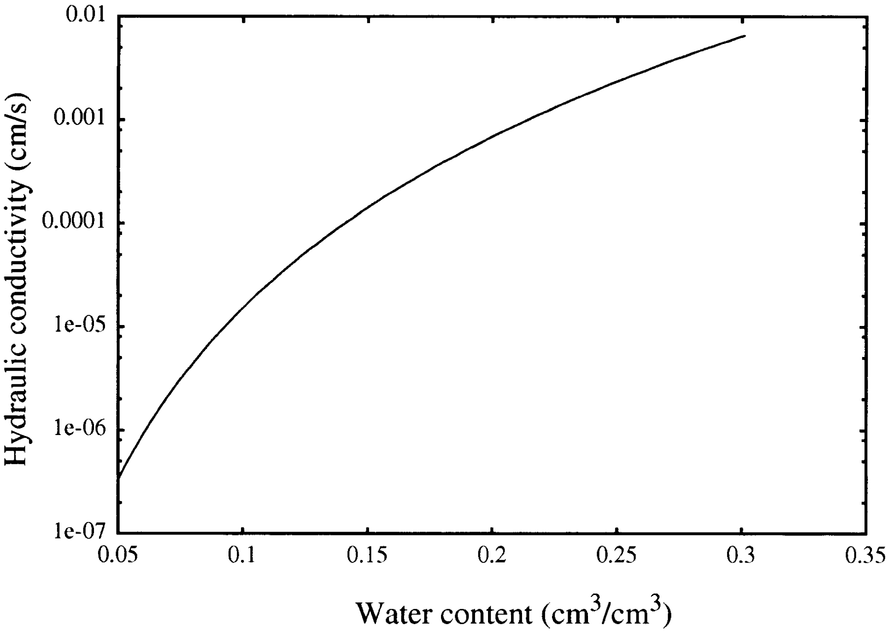

Fig. 3. Hydraulic conductivity—water content relationship.

$$K_1(\theta) = a\theta^b \tag{24}$$

with $a = 4.88$ cm s^{-1} and $b = 5.509$.

The time history of water pressure head applied at the bottom of the column is shown in Fig. 4. In the finite element model, 60 3-node 1D elements were used to obtain water content variation along the column at different times. A constant time step ($\Delta t = 60$ s) was used. An iterative procedure similar to the previous example was adopted at each time step until convergence is reached. Of the problem discussed here, the hysteretic path involves only the main drying curve and primary wetting scanning curve. A hysteresis index was used in the computational algorithm to identify the drying or wetting states and thereby choose proper scanning curves for each node at every time step. The finite element solutions for water content have been compared with measured values at the five different time instances ($t = 0$, 45, 68, 90 and 125 min). Predictions using the hysteretic model are in general agreement considering the approximations in the soil property data. Solutions at two typical time instances, $t = 68$ min corresponding to early rewetting and $t = 125$ min (last measured time), are plotted in Fig. 5 and compared with the experimental results.

The same problem was also solved by using the main wetting curve or the main drying curve respectively without considering the hysteretic effects. The corresponding solutions are plotted in Fig. 5 for comparison. It is noticed that the solutions with hysteretic effect generally agree with the experimental results at all the measured time instances. At $t = 68$ min, the top half of the column is still in the drying phase, therefore the water contents are almost the same, as predicted by using the main drying curve only. On the other hand, the bottom half of the column has entered

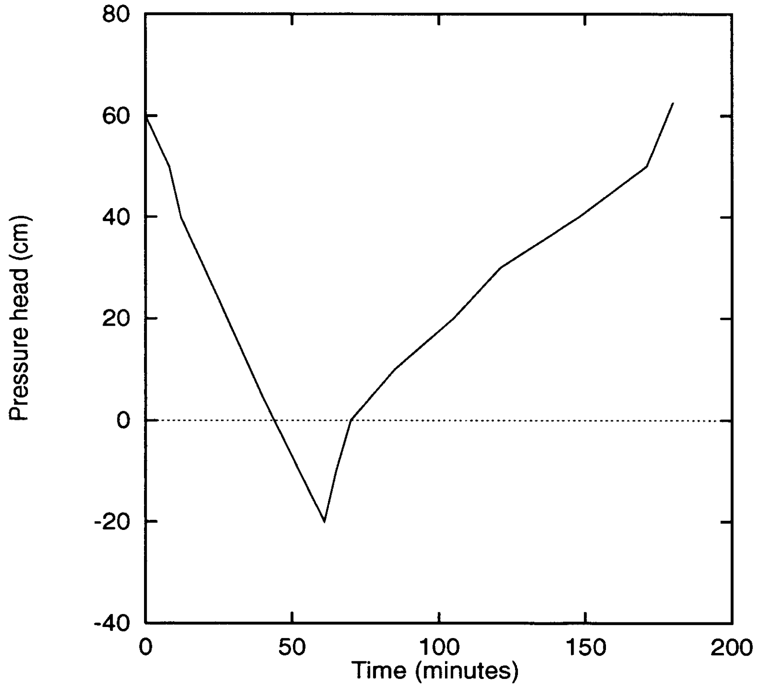

Fig. 4. Time dependent boundary condition imposed at the bottom of the column (Gillham et al., 1979).

into the wetting phase and the primary wetting scanning curve has to be followed. The water content is lower than that predicted by using the main drying curve only. By using the main wetting curve only, much lower water contents are predicted than those corresponding to hysteretic solutions at 68 min. At $t = 125$ min, most parts of the column have entered into the wetting phase and thereby have increased water content. Only a small area near the top is still in the drying phase and the water content is further decreased. The results predicted using only the main drying curve overestimate the water content significantly. The results predicted using only the main wetting curve appears to be more reasonable than using only the main drying curve. This is because most part of the column is in the wetting phase. It should be noted that more significant errors can be expected for problems involving repeated wetting and drying if only the main wetting curve or main drying curve is used.

4.3. *Case* 3

In the third example, the finite element code is applied to simulate the heating experiment conducted by Villar et al. (1993). An unsaturated cylindrical soil sample with 15 cm diameter, 14.6 cm height was heated using a 1.0 cm diameter, 1.5 cm high heater embedded at the top of the soil sample as shown in Fig. 6. In this axisymmetric problem, ninety three-node triangular axisymmetric elements are used to model the sample. The initial temperature, porosity and degree of saturation of the sample are 20°C, 0.422 and 50%, respectively. Initial water pressure (suction) is -130 MPa, and the initial air pressure (atmospheric) is 98 kPa. The outer boundary BCD is fixed (zero

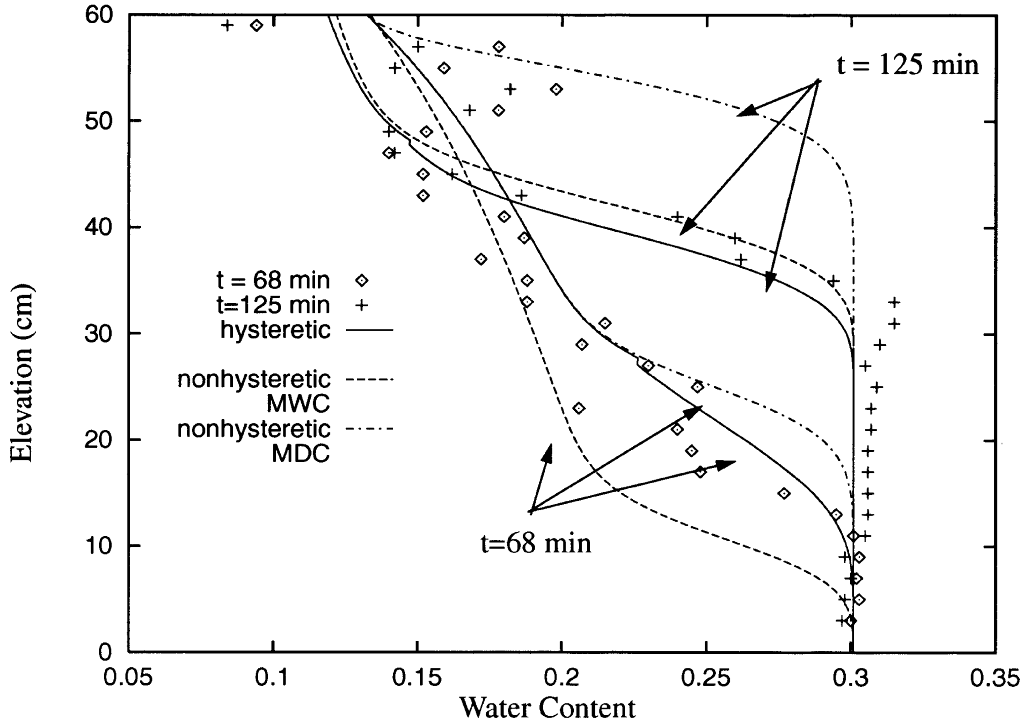

Fig. 5. Simulated water content profiles for slow drainage-rewet experiment (Gillham et al., 1979).

displacement) in both normal and tangential directions, and is impermeable. The boundary BCD is also subjected to a constant temperature increase of 10°C to give a constant temperature of 30°C. At the outer boundary of the heater, temperature is maintained at 100°C resulting in an 80°C temperature increase. The top surface AB is thermally insulated, impermeable to liquid water and water vapour, and the air pressure is atmospheric.

The heater is treated as a rigid impermeable body. Steady-state was observed after 20 h in the experimental study. The material properties relevant to the experiment are summarized in Table 1. These properties are obtained from the experimental work reported by Villar and Martin (1993) and Villar et al. (1993), and the numerical modeling by Thomas and He (1995). The coefficients D_T and D_c associated with thermo-osmosis and thermal-filtration are not available for the soil used in the experiment and have been set to zero.

The conductivities of liquid water and air are given by Villar and Martin (1993) and Fredlund and Rahardjo (1993):

$$K_l = 1.2\times 10^{-16}\left(\frac{S_l-0.05}{1-0.05}\right)^3 10^{5e}(\mathrm{m\,s^{-1}}) \tag{25}$$

$$K_a = \frac{3.0\times 10^{-9}[e(1-S_l)]^4}{1.846\times 10^{-5}}(\mathrm{m\,s^{-1}}) \tag{26}$$

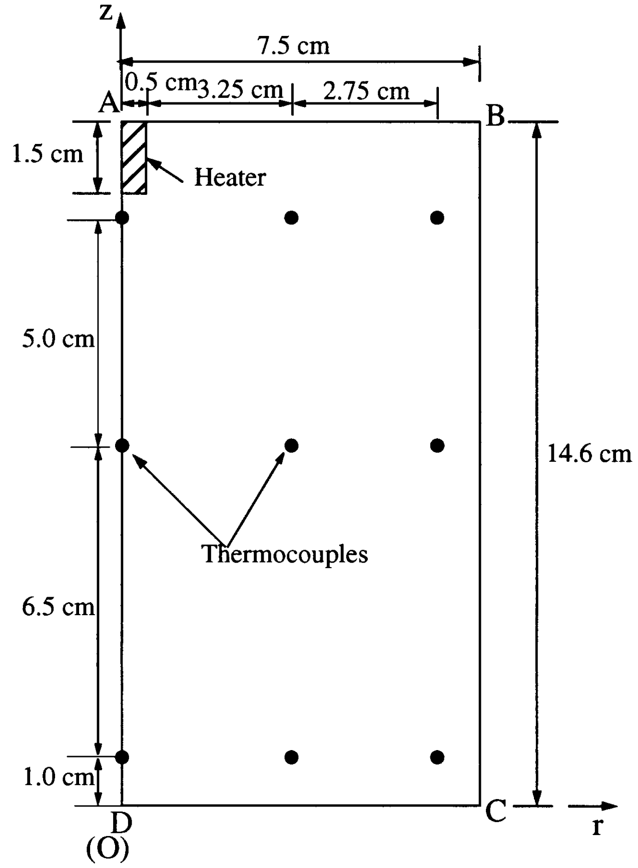

Fig. 6. Geometry of Villar's experimental sample.

Figure 7 shows predicted contours of temperature at different times. At very early times ($t < 1$ h), two thermal fronts propagate through the sample: one from the embedded heater at the top and another from the outer boundary BCD. As time progresses, the thermal front from the heater approaches the boundary BCD and the heat flow from the boundary to the sample vanishes. The dominant thermal front is due to the embedded heater. These trends are clearly seen in the temperature contours at $t = 0.5$, 1.0 and 5.0 h in Fig. 7. Steady-state conditions for temperature are reached for $t \geqslant 5$ h, with the corresponding temperature contours having the typical bulb shape observed in uncoupled heat transfer problems. Steady-state temperatures at different locations observed in the experiment are also shown in Fig. 7 at $t = 20$ h. Good agreement is noticed except at the thermocouple located immediately below the heater. Differences between experimental and numerical results in the vicinity of the heater can be due to imperfect contact between the heater and soil, and heat loss through the top boundary.

Figure 8 shows calculated contours of degree of water saturation at different times. Water is continuously driven away from the heater until a steady-state condition is reached at 200 h. There is negligible moisture movement from the outer boundary at early times due to initial heating of

Table 1
Material parameters

Parameter (unit)	Value	Parameter (unit)	Value
α_l [°C^{-1}]	3.0×10^{-4}	C_s [J kg^{-1} °C^{-1}]	800
T_0 [K]	293	C_l [J kg^{-1} °C^{-1}]	4186
β_l [Pa]	3.3×10^{9}	C_v [J kg^{-1} °C^{-1}]	1870
H	0.02	C_{da} [J kg^{-1} °C^{-1}]	1000
E [Pa]	5.7×10^{8}	λ_{dry} [J s^{-1} m^{-1} °C^{-1}]	0.3
v	0.2	λ_{sat} [J s^{-1} m^{-1} °C^{-1}]	1.3
B_1 [Pa^{-1}]	1.34×10^{-10}	R_v [J kg^{-1} °C^{-1}]	461.5
α [°C^{-1}]	3.0×10^{-4}	R_{da} [J kg^{-1} °C^{-1}]	287.1
B_2 [Pa^{-1}]	6.0×10^{-10}	ρ_{l0} [kg m^{-3}]	998
B_3 [Pa^{-1}]	7.0×10^{-10}	ρ_{s0} [kg m^{-3}]	2780
B_4	2.4×10^{-4}	L_0 [J kg^{-1}]	2.4×10^{6}
θ_0	0.211	H_w [J m^{-2}]	1.0
n_0	0.422	δ [m]	1.0×10^{-9}
τ	2/3	S [m^{-1}]	1.0×10^{7}

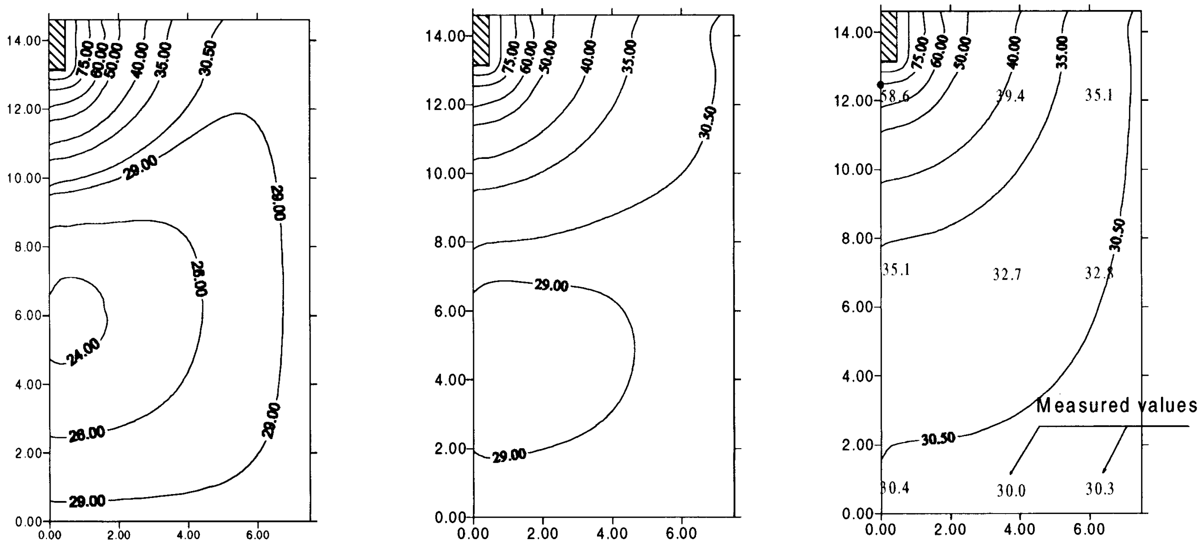

a) t = 0.5 hour b) t = 1 hour c) t = 5 hours

Fig. 7. Temperature contours at different times.

the boundary. Initially (t = 1 h) the soil dries near the heater (Fig. 8a) and later moves to the boundary BCD as expected (Fig. 8d). The flow of water in both radial and vertical directions is seen in Fig. 8. The water movement is slow due to the low permeability of the medium. As a consequence, steady-state conditions for degree of water saturation are attained much later than

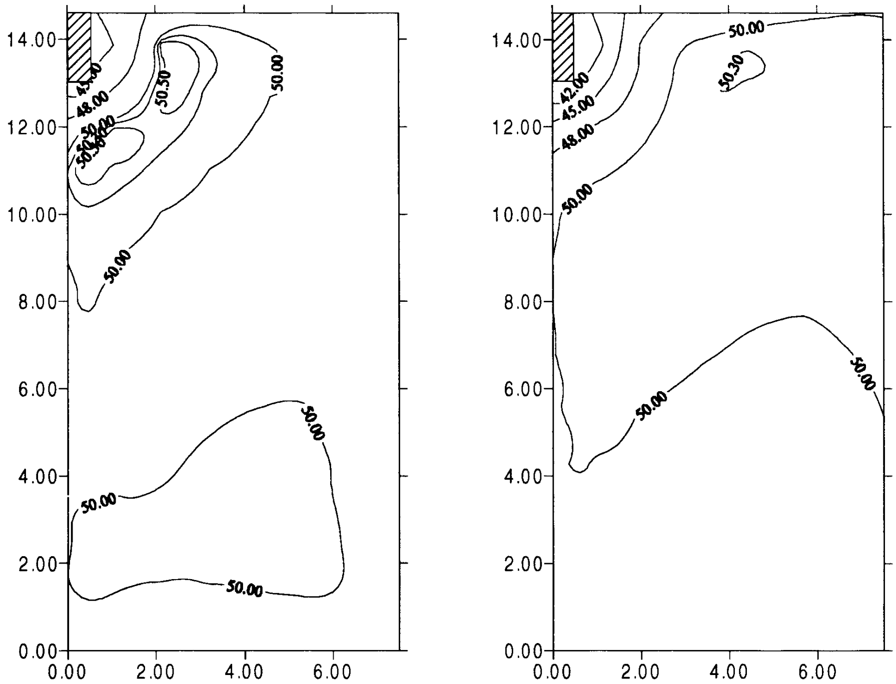

a) t=1 hour

b) t=5 hours

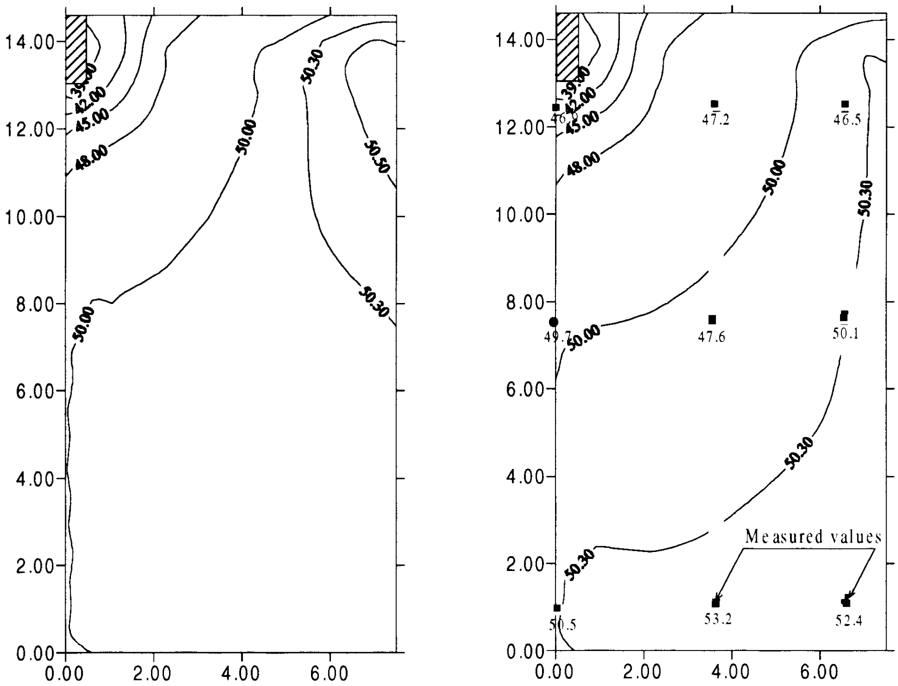

c) t=20 hours

d) t=200 hours

Fig. 8. Degree of water saturation contours at different times.

for temperature. An appreciable reduction in degree of saturation is noted only in the immediate vicinity of the heater. Since all the boundaries are impermeable there is no water loss—a decrease in the degree of water saturation in one region results in an increase elsewhere in the sample. An increase in degree of saturation is therefore observed near the boundary BCD. This increase is quite small since the volume of the dried soil is only a small fraction of the sample.

Overall the predicted distribution in Fig. 8 has the correct trends. Figure 8d also shows steady-state degrees of saturation re-interpreted by Thomas and He (1995) from the experiments conducted by Villar et al. (1993). The trend is reasonably matched although the experimental results show more drying near the heater and more wetting near the base of the sample. It should be emphasized that the degree of saturations observed in the experiment may not be the steady-state values as the steady-state for moisture flow occurs much later than the heat flow. It is also not clear from Villar's experiments how the condition for steady-state of the degree of saturation was actually verified. It is relatively easy in the experiment to verify the steady-state of temperature from readings of the thermocouples. However, the same is not true for degree of saturation which usually involves disassembling of the experiment and cooling, with consequent moisture redistribution.

Figure 9 shows the contours of capillary pressure at different times. The suction (negative capillary pressure) continues to increase near the heater until steady-state is reached at 200 h, the same time required for degree of saturation. In line with the experimental evidences, areas with higher degree of saturation have lower suctions. The change in air pressure is found to be negligible.

4.4. *Case* 4

The next problem considered is heating of a thick cylinder. Plane strain behaviour with radial symmetry is assumed. The dimensions of the cylinder are selected to be similar to those associated with potential field situations involving heat emitting wastes. The geometry of the thick cylinder is shown in Fig. 10 and $a = 0.3165$ m, $b = 0.62$ m. The initial and boundary conditions can be described as following. Initially, the medium is at 20°C uniform temperature with 0.422 porosity and 50% degree of water saturation. The initial water pressure is -130 MPa and air pressure is 98 kPa. Both inner and outer boundaries are fixed and impermeable. At the inner boundary the medium is suddenly subjected to 60°C temperature increase. The temperature at the outer boundary is kept unchanged. The material properties are the same as those in Case 3 and D_T and D_c are set to zero.

Figure 11 shows capillary pressure, degree of saturation, radial displacement and temperature at different times. Capillary pressure near the heated inner surface decreases with time (becomes more negative) due to the outward movement of the water. The trend of water movement in the thick cylinder can be seen from Fig. 11b where the degree of saturation is plotted for different times. The water movement is confined to the immediate vicinity of the inner surface ($0.3 < r < 0.4$) at initial times ($t \leqslant 5$ h). Note the interesting short-term increases in degrees of saturation close to the heater associated with early movement of water from areas first heated. Such increases have been observed in both laboratory and field experiments, and have been difficult to explain. As times progress, the degree of saturation near the heater decreases by nearly twenty percent and increases at the outer boundary by approximately five percent. Since both inner and outer boundaries are impermeable, water does not escape out of the cylinder. Any decrease in one region is

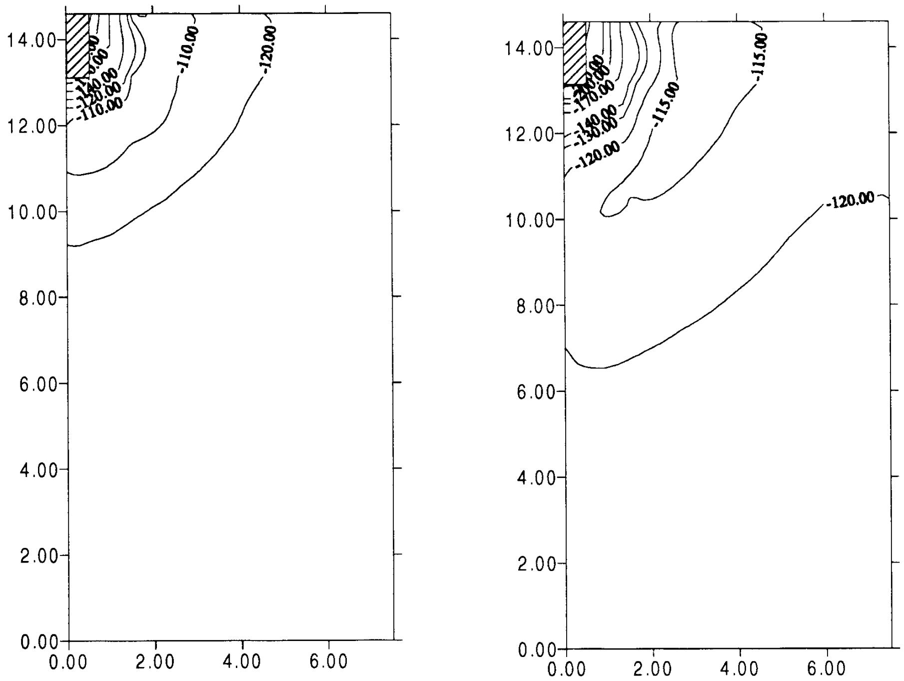

a) t=1 hour

b) t=5 hours

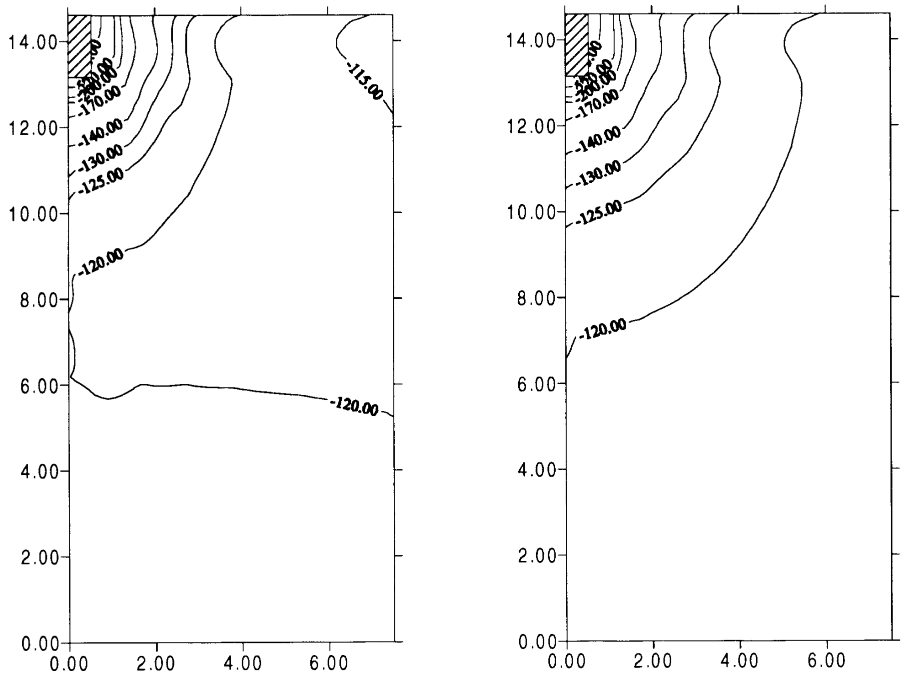

c) t=20 hours

d) t=200 hours

Fig. 9. Capillary pressure contours at different times.

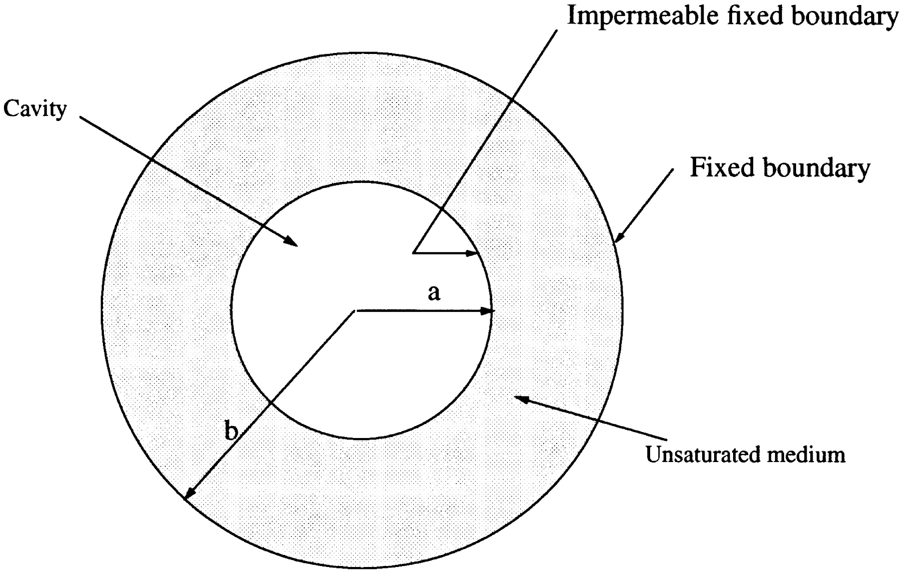

Fig. 10. Geometry of thick cylinder problem.

matched by an increase at other locations. The increase of degree of saturation near the outer boundary also results in an increase of capillary pressure which becomes less negative. Steady-state conditions for capillary pressure and degree of saturation are reached after 1000 h. Air pressure changes are found to be negligible.

Figure 11c shows the distribution of radial displacement. Initially displacement increases in the immediate vicinity of the inner boundary due to thermal expansion of water caused by heating. The heating also initiates a slow movement of water away from the inner boundary. The total effect of these two processes is an initial increase in the displacement followed by a decrease. Finally there is compressibility close to the heater due to drying and shrinkage. Displacements near the outer boundary also increase initially with time due to heating and decrease thereafter as the capillary pressures increase. Figure 11d shows temperature distribution with time. The temperature rises rapidly with time and the steady-state is reached at $t = 50$ h. The steady-state temperature distribution agrees closely with the uncoupled solution for temperature distribution in a thick cylinder (Carslaw and Jaegar, 1960). Note that these insights which agree qualitatively with field results described by Graham et al. (1996) cannot be predicted by existing constant-volume models.

The importance of coupled flow terms associated with the phenomenological coefficients D_T and $D_c = [(T+T_0)D_T]$ (thermo-osmosis and thermal-filtration type effects) in eqns (5) and (12) is investigated next. Only limited data are available for the phenomenological coupling coefficients (D_T). The effect has therefore been investigated assuming different values for D_T based on range of values reported in literature for some soils. Figure 12 shows solutions for the thick cylinder problem (Fig. 10) with $D_T = 2.7 \times 10^{-12}$ m^2 s^{-1} °C^{-1} which is one-hundredth of the values used by Carnahan (1984) for clay from the experiments conducted by Srivastava and Avasthi (1975).

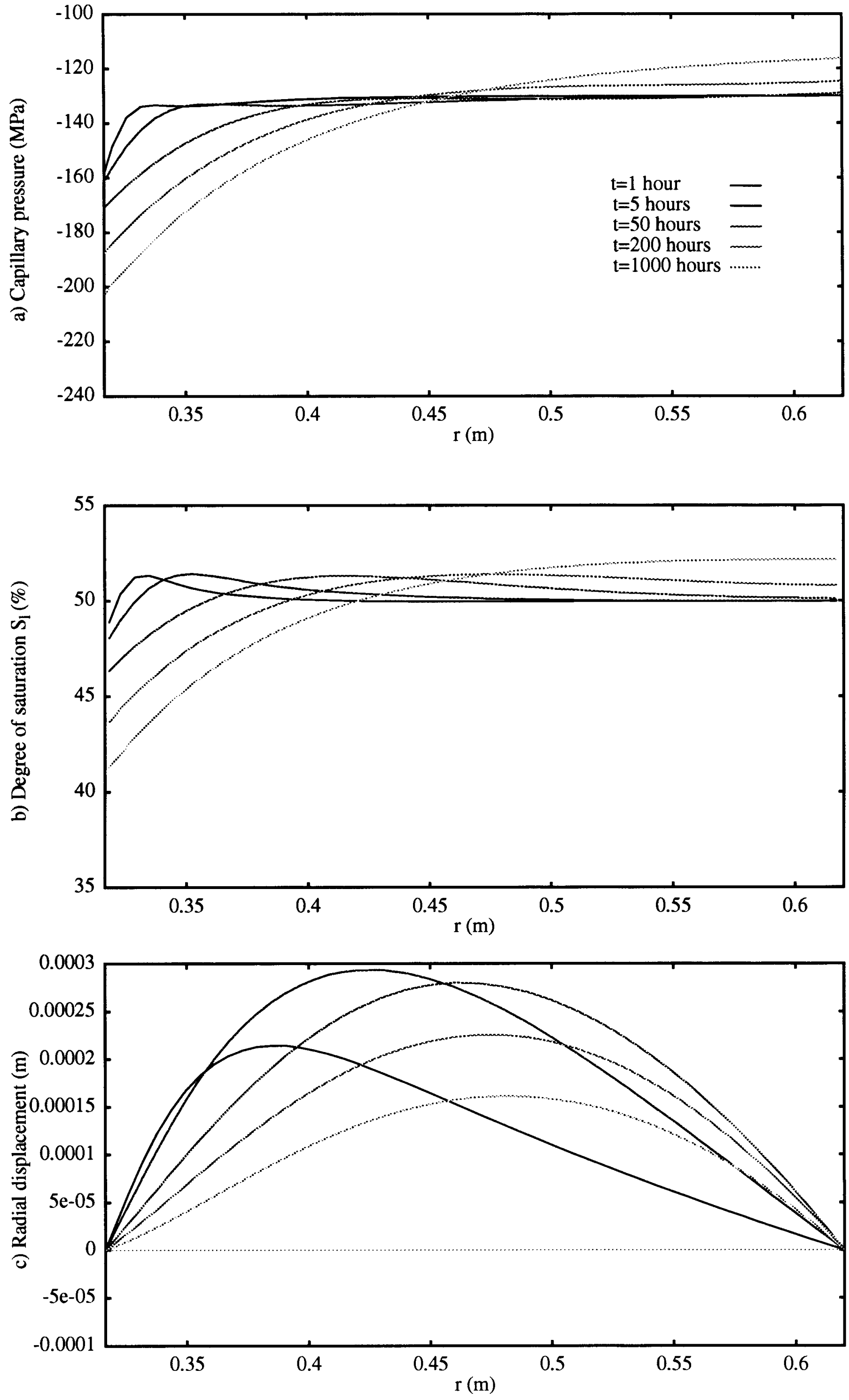

Fig. 11. Coupled fields in a thick cylinder due to heating ($D_T = 0$).

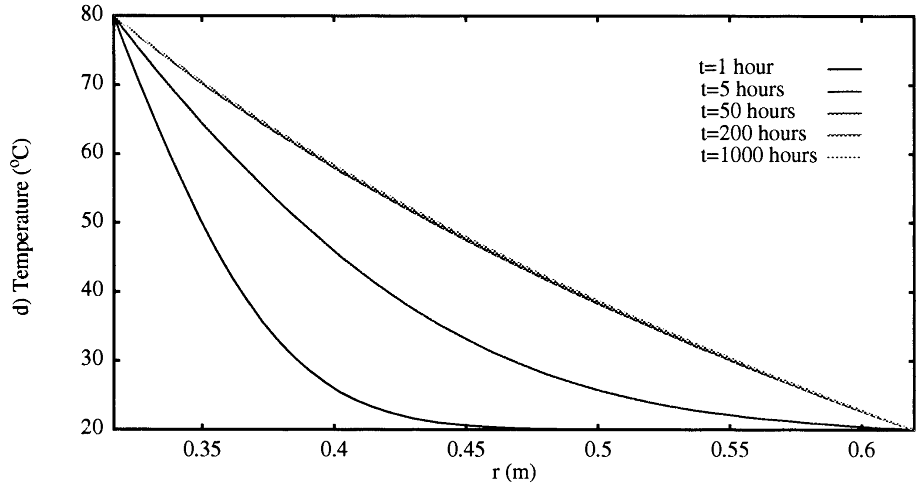

Fig. 11 (*continued*).

Figure 13 shows the solutions for $D_T = 5.4 \times 10^{-12}$ m^2 s^{-1} °C^{-1}. These coefficients are twice the values used in Fig. 12.

Comparison of Figs 11, 12 and 13 shows that the additional coupled flow terms have significant effects on the distributions of capillary pressure and degree of saturation. It is found that the major influence comes from D_T in eqn (5). Steady state capillary pressure on the inner boundary increases from -200 to -240 MPa when D_T changes from zero to 5.4×10^{-12} m^2 s^{-1} °C^{-1}. An increase of 15% in outer boundary capillary pressure is also noted. In addition, the degree of water saturation at the inner surface decreases from 41.2 to 35%, and that at the outer surface increases from 52 to 55%. Therefore as mentioned by Horseman and McEwen (1996), therm-osmosis type coupling has the potential to dry the near-field and increase the movement of water away from heat generating waste. Important differences are also noted in steady-state radial displacement distributions. Comparison of Figs 11 and 13 shows that for larger values of D_T shrinkage occurs near the heater at steady state due to increased drying. The magnitude of steady-state displacement also decreases with increasing D_T. The displacements at early times ($t \leqslant 50$ h) are not influenced by the presence of additional flow terms. It appears that the displacement during $0 < t < 50$ h is primarily due to heating of the medium. The effects due to water movement and capillary pressure change comes into effect only after $t > 50$ h.

4.5. *Case* 5

The final example involves the case of the thick cylinder in Fig. 10 being subjected to heating at the inner boundary and infiltration at the outer boundary. Such a problem reflects the practical problem of groundwater movement into a heat emitting waste repository. It is expected that drying and rewetting would occur near the heated boundary in this case. Strictly speaking, such a situation would require the consideration of hysteresis in hydraulic properties as in the case of soil column problem considered previously. However, due to lack of experimental data hysteresis is neglected and material properties identical to those given in Case 3 are used. A capillary pressure of -70

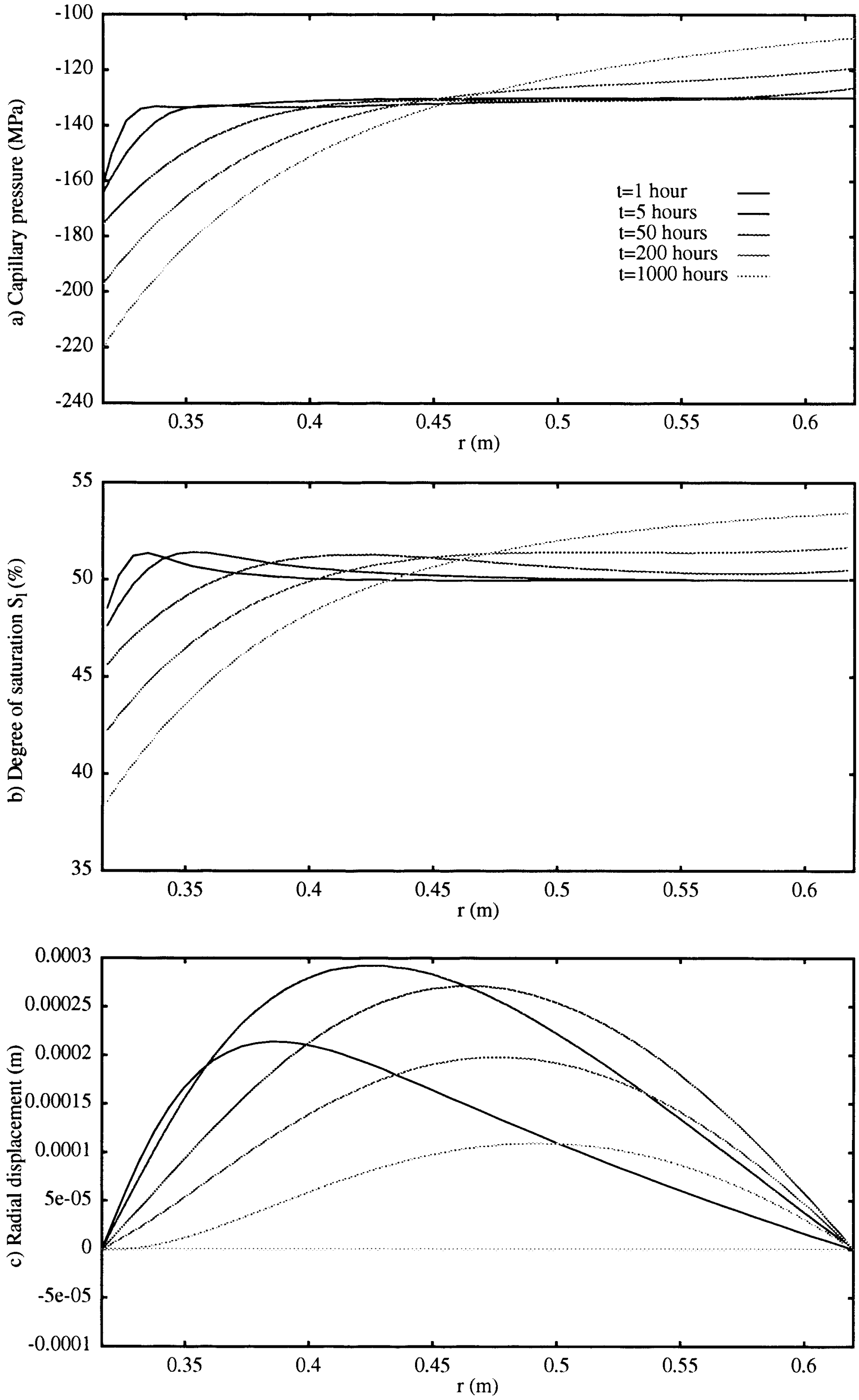

Fig. 12. Coupled fields in a thick cylinder due to heating ($D_T = 2.7 \times 10^{-12}$ m^2 s^{-1} °C^{-1}).

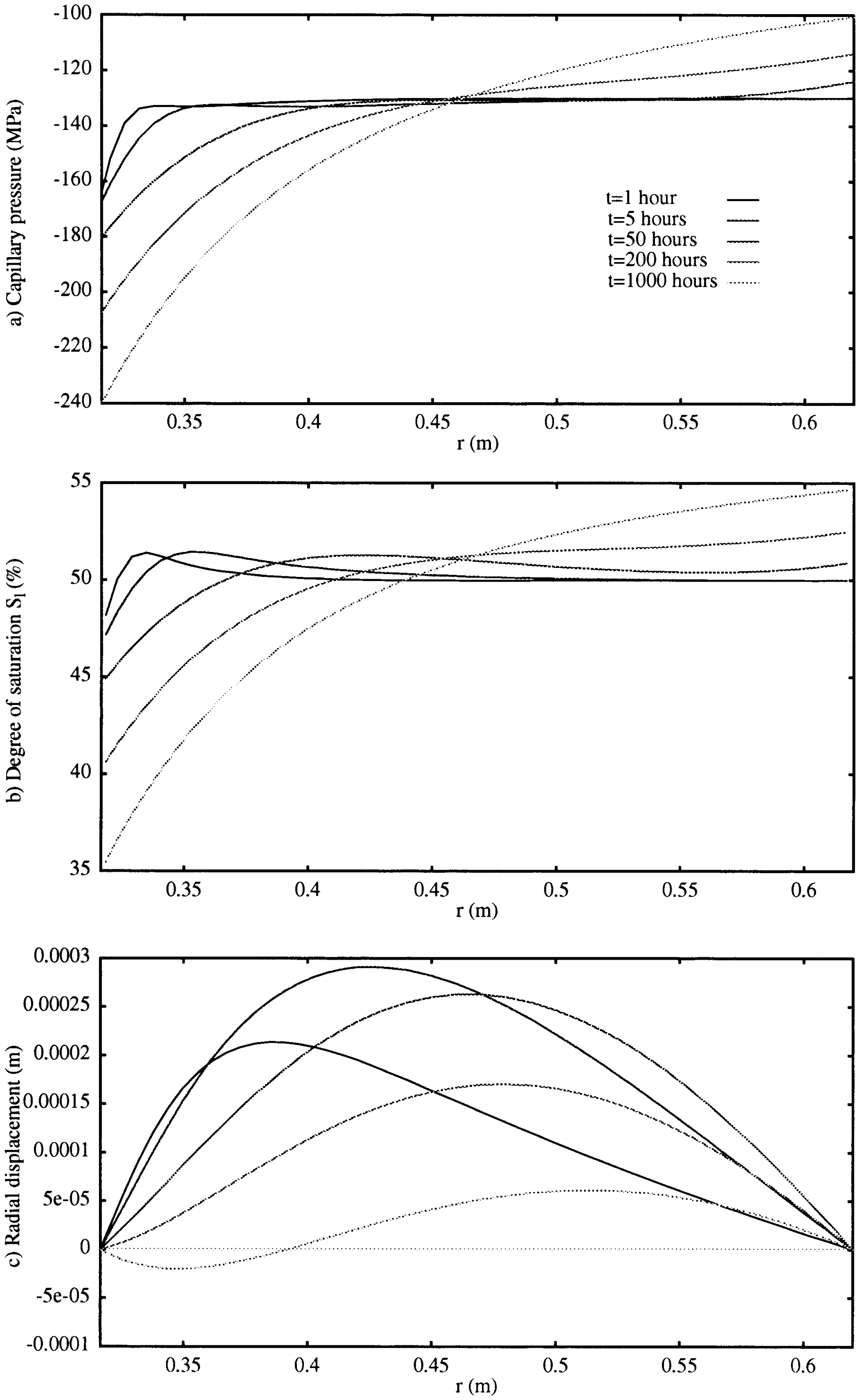

Fig. 13. Coupled fields in a thick cylinder due to heating ($D_T = 5.4 \times 10^{-12}$ m^2 s^{-1} °C^{-1}).

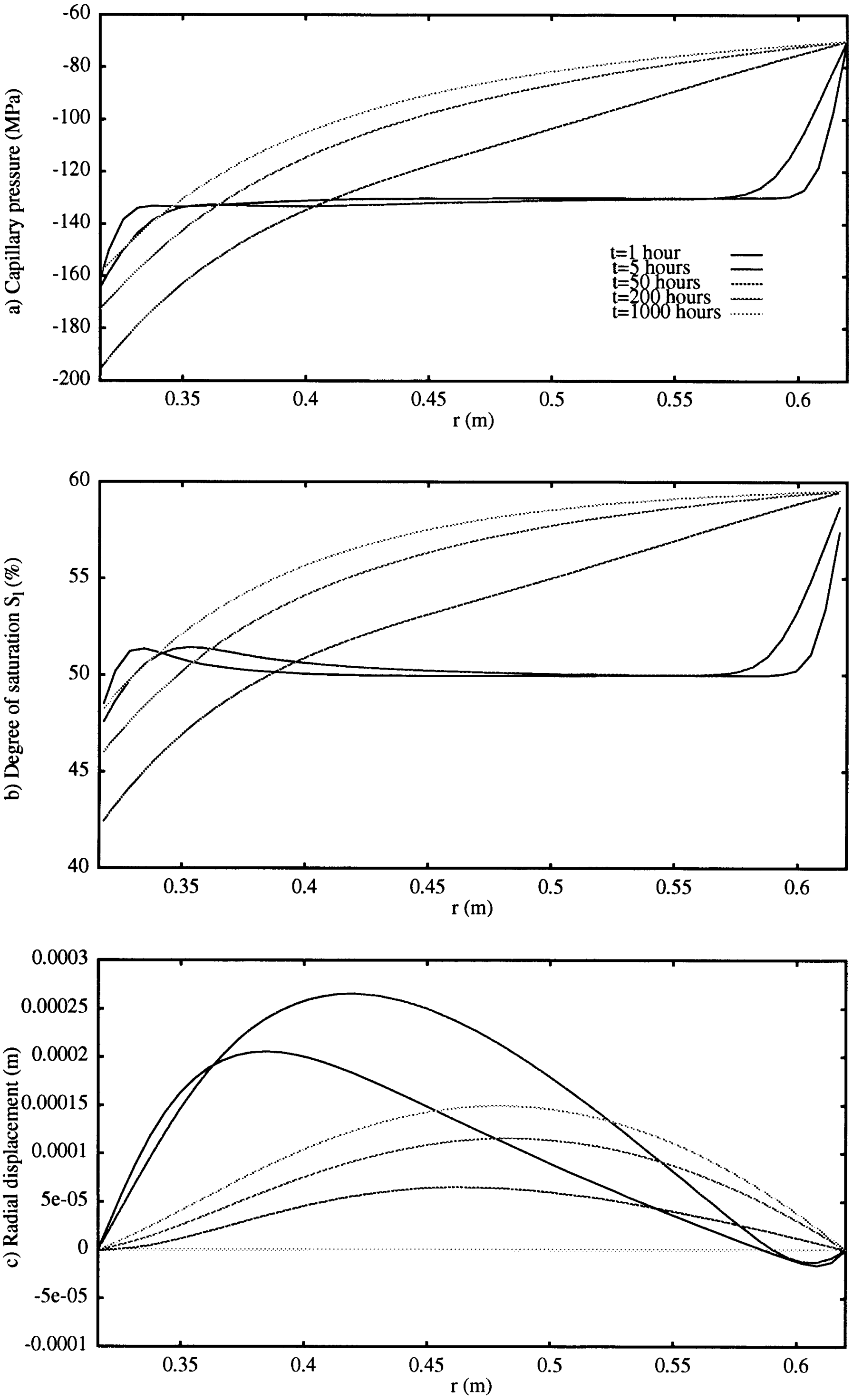

Fig. 14. Coupled fields in a thick cylinder due to heating and infiltration ($D_T = 2.7 \times 10^{-12}$ m^2 s^{-1} °C^{-1}).

MPa (suction) (equivalent to constant volumetric water content of 25.1%) is applied on the outer boundary. The other boundary and initial conditions are unchanged from the previous thick cylinder example.

Figure 14 shows capillary pressure, degree of saturation and radial displacement at different times for $D_T = 2.7 \times 10^{-12}$ m^2 s^{-1} °C^{-1}. At early times ($t < 5$ h), the effects of heating and infiltration are localized. The capillary pressure and the degree of saturation decrease near the heater and increase near the outer boundary. As time progresses ($t \geqslant 50$ h) more flow of water takes place inwards from the outer boundary. Drying of the medium near the heated boundary occurs until about 50 h. Thereafter the degree of saturation at the heated end begins to increase due to inward water flow. Note that the inner boundary is impermeable. The capillary pressure changes shown in Fig 14a closely follow the changes in degree of saturation. Steady-state conditions of capillary pressure and degree of saturation are observed around 1000 h. Initial displacement profiles are identical to Fig. 13 except near the outer boundary where the influence of infiltration is evident. The temperature distribution in the cylinder is almost identical to that shown in Fig. 11d.

5. Conclusions

A variety of problems involving heating and infiltration of unsaturated media have been successfully simulated by using a new hygro-thermo-mechanical model. Stable numerical solutions were obtained for all field variables using a Galerkin type finite element formulation of the mathematical model. Non-linear mechanical behaviour of the medium was not considered due to lack of experimental data under hygo-thermo-mechanical loading. However, important non-linear dependencies for moisture, air and heat flow including hysteresis of hydraulic properties are included in the present modeling. Comparisons with experimental results reported by Gillham et al. (1979) and Villar et al. (1993) show quite good agreement. However, experimental results show more drying near a heater. This may be a consequence of a thermo-osmosis type effect often neglected in mathematical modeling. The consideration of absorbed liquid flow due to thermal gradients in a heated confined cylinder results in more drying and reduction in capillary pressure. A reduction in steady-state radial displacement and shrinkage near the heater are also noted due to the inclusion of additional liquid flow terms. Time histories of temperature are nearly identical to those obtained using the uncoupled heat transfer equations. Air pressure change due to heating is negligible. Coupled fields predicted by the present model agree qualitatively with laboratory and field results and show important features that cannot be predicted by existing constant volume models.

Acknowledgements

The work presented in this paper was supported by the Natural Sciences and Engineering Research Council of Canada, and Atomic Energy Canada Ltd.

Appendix 1

The coefficients used in eqns (14)–(16) are expressed as follows:

$$L_{11} = \rho_1(\theta + B'_2); \quad L_{12} = \rho_1 B'_3 + \rho_{10}\beta_1\theta$$

$$L_{13} = \rho_{10}\beta_1\theta; \quad L_{14} = \rho_1 B'_4 - \rho_{10}\alpha_1\theta$$

$$L_{21} = \rho_v(1-\theta-B'_2); \quad L_{22} = -\rho_v B'_3 + (n-\theta)\frac{D'_1}{D^*}$$

$$L_{23} = (n-\theta)\frac{D'_2}{D^*}; \quad L_{24} = -\rho_v B'_4 + (n-\theta)\frac{D'_3}{D^*}$$

$$L_{31} = \rho_{da}[1-(1-H)(\theta+B'_2)]$$

$$L_{32} = -\left\{(1-H)\,\rho_{da}B'_3 + [n-(1-H)\theta]\frac{R_v D_1^*}{R_{da}D^*}\right\}$$

$$L_{33} = [n-(1-H)\theta]\left[\frac{1}{R_{da}(T+T_0)} - \frac{R_v D_2^*}{R_{da}D^*}\right]$$

$$L_{34} = -\left\{(1-H)\rho_{da}B'_4 + [n-(1-H)\theta]\left[\frac{p_a}{R_{da}(T+T_0)^2} + \frac{R_v D_3^*}{R_{da}D^*}\right]\right\}$$

$$L_{41} = \left[\theta + B'_2\left(1-\frac{\theta}{\delta S}\right)\right]\frac{H_w}{\delta}\mathrm{e}^{-\theta/\delta S} - (T+T_0)\,K\alpha + C_1 T L_{11} + (L_0 + C_v T)L_{21} + C_{da}TL_{31}$$

$$L_{42} = B'_3\left(1-\frac{\theta}{\delta S}\right)\frac{H_w}{\delta}\mathrm{e}^{-\theta/\delta S} + C_1 T L_{12} + (L_0 + C_v T)L_{22} + C_{da}TL_{32}$$

$$L_{43} = C_1 T L_{13} + (L_0 + C_v T)L_{23} + C_{da}TL_{33}$$

$$L_{44} = (\rho C)_m^* + B'_4\left(1-\frac{\theta}{\delta S}\right)\frac{H_w}{\delta}\mathrm{e}^{-\theta/\delta S} + C_1 T L_{14} + (L_0 + C_v T)L_{24} + C_{da}TL_{34}$$

$$D_1^* = D^*\rho_v\left[\frac{1}{\rho_1 R_v(T+T_0)} - \frac{p_c\rho_{1o}\beta_1}{\rho_1^2 R_v(T+T_0)}\right]; \quad D_2^* = -D^*\frac{\rho_v p_c \rho_{1o}\beta_1}{\rho_1^2 R_v(T+T_0)}$$

$$D_3^* = D^*\left[h\frac{\mathrm{d}\rho_0}{\mathrm{d}\,T} - \frac{\rho_v p_c}{\rho_1 R_v(T+T_0)^2} + \frac{\rho_v p_c \rho_{1o}\alpha_1}{\rho_1^2 R_v(T+T_0)}\right]$$

$$D_{c2}^* = (\rho_1 K_1 C_1 + D_1^* C_v + C_{da}K_1\rho_{da}H)\,T + L_0 D_1^* + D_c$$

$$D_{a2}^* = [\rho_1 K_1 C_1 + (\rho_v K_a + D_2^*)C_v + C_{da}\rho_{da}(K_a + HK_1)]\,T + L_0(\rho_v K_a + D_2^*) + D_c$$

$$D_{T2}^* = (\rho_1 D_T C_1 + D_3^* C_v + C_{da}D_T\rho_{da}H)\,T + \lambda + L_0 D_3^*$$

where ρ_{l0} is the initial density of liquid water, α_l is thermal expansion coefficient of liquid water, β_l is the compressibility of liquid water, n is porosity, ρ_0 is density of saturated water vapour, R_{da} and R_v are specific gas constants for dry air and water vapour respectively, S is specific surface of the material, H_w and δ are material constants for differential heat of wetting, $B_2' = B_2K$, $B_3' = B_3 - B_1B_2K$, $B_4' = B_4 - \alpha B_2K$; and

$$(\rho C)_m^* = \frac{[\rho_s C_s + \rho_l(1+e)\theta C_l + \rho_v(e-(1+e)\theta)C_v + \rho_{da}(e-(1-H)(1+e)\theta)C_{da}]}{(1+e)}$$

Appendix 2

The matrices **G** and **K** and vectors **X** and **F** in eqn (18) are given by

$$\mathbf{G} = \begin{bmatrix} 0 & 0 & 0 & 0 \\ \mathbf{G}_{21} & \mathbf{G}_{22} & \mathbf{G}_{23} & \mathbf{G}_{24} \\ \mathbf{G}_{31} & \mathbf{G}_{32} & \mathbf{G}_{33} & \mathbf{G}_{34} \\ \mathbf{G}_{41} & \mathbf{G}_{42} & \mathbf{G}_{43} & \mathbf{G}_{44} \end{bmatrix}; \quad \mathbf{K} = \begin{bmatrix} \mathbf{K}_{11} & \mathbf{K}_{12} & \mathbf{K}_{13} & \mathbf{K}_{14} \\ 0 & \mathbf{K}_{22} & \mathbf{G}_{23} & \mathbf{G}_{24} \\ 0 & \mathbf{K}_{32} & \mathbf{K}_{33} & \mathbf{K}_{34} \\ 0 & \mathbf{K}_{42} & \mathbf{K}_{43} & \mathbf{K}_{44} \end{bmatrix};$$

$$\mathbf{X} = \begin{Bmatrix} \hat{\mathbf{U}}(t) \\ \hat{\mathbf{P}}_c(t) \\ \hat{\mathbf{P}}_a(t) \\ \hat{\mathbf{T}}(t) \end{Bmatrix}; \quad \mathbf{F} = \begin{Bmatrix} \mathbf{F}_1 \\ \mathbf{F}_2 \\ \mathbf{F}_3 \\ \mathbf{F}_4 \end{Bmatrix}$$

where

$$\mathbf{G}_{21} = \int_\Omega \mathbf{N}^T(\mathrm{L}_{11} + \mathrm{L}_{21})\mathbf{mB}\,\mathrm{d}\Omega, \quad \mathbf{G}_{22} = \int_\Omega \mathbf{N}^T(\mathrm{L}_{12} + \mathrm{L}_{22})\mathbf{N}\,\mathrm{d}\Omega,$$

$$\mathbf{G}_{23} = \int_\Omega \mathbf{N}^T(\mathrm{L}_{13} + \mathrm{L}_{23})\mathbf{N}\,\mathrm{d}\Omega, \quad \mathbf{G}_{24} = \int_\Omega \mathbf{N}^T(\mathrm{L}_{14} + \mathrm{L}_{24})\mathbf{N}\,\mathrm{d}\Omega,$$

$$\mathbf{G}_{31} = \int_\Omega \mathbf{N}^T\mathrm{L}_{31}\mathbf{mB}\,\mathrm{d}\Omega, \quad \mathbf{G}_{32} = \int_\Omega \mathbf{N}^T\mathrm{L}_{32}\mathbf{N}\,\mathrm{d}\Omega, \quad \mathbf{G}_{33} = \int_\Omega \mathbf{N}^T\mathrm{L}_{33}\mathbf{N}\,\mathrm{d}\Omega,$$

$$\mathbf{G}_{34} = \int_\Omega \mathbf{N}^T\mathrm{L}_{34}\mathbf{N}\,\mathrm{d}\Omega, \quad \mathbf{G}_{41} = \int_\Omega \mathbf{N}^T\mathrm{L}_{41}\mathbf{mB}\,\mathrm{d}\Omega, \quad \mathbf{G}_{42} = \int_\Omega \mathbf{N}^T\mathrm{L}_{42}\mathbf{N}\,\mathrm{d}\Omega,$$

$$\mathbf{G}_{43} = \int_\Omega \mathbf{N}^T\mathrm{L}_{43}\mathbf{N}\,\mathrm{d}\Omega, \quad \mathbf{G}_{44} = \int_\Omega \mathbf{N}^T\mathrm{L}_{44}\mathbf{N}\,\mathrm{d}\Omega, \quad \mathbf{K}_{11} = \int_\Omega \mathbf{B}^T\mathbf{DB}\,\mathrm{d}\Omega,$$

$$\mathbf{K}_{12} = -\int_\Omega \mathbf{B}^T\mathrm{K}\mathrm{B}_1\mathbf{m}^T\mathbf{N}\,\mathrm{d}\Omega, \quad \mathbf{K}_{13} = -\int_\Omega \mathbf{B}^T\mathbf{m}^T\mathbf{N}\,\mathrm{d}\Omega, \quad \mathbf{K}_{14} = -\int_\Omega \mathbf{B}^T\mathrm{K}\alpha\mathbf{m}^T\mathbf{N}\,\mathrm{d}\Omega,$$

$$\mathbf{K}_{22} = \int_\Omega \nabla\mathbf{N}^T(\rho_l K_l + D_1^*)\nabla\mathbf{N}\,\mathrm{d}\Omega, \quad \mathbf{K}_{23} = \int_\Omega \nabla\mathbf{N}^T(\rho_v K_a + \rho_l K_l + D_2^*)\nabla\mathbf{N}\,\mathrm{d}\Omega,$$

$$\mathbf{K}_{24} = \int_\Omega \nabla\mathbf{N}^T(\rho_l D_T + D_3^*)\nabla\mathbf{N}\,\mathrm{d}\Omega, \quad \mathbf{K}_{32} = \int_\Omega \nabla\mathbf{N}^T H\rho_{da} K_l \nabla\mathbf{N}\,\mathrm{d}\Omega,$$

$$\mathbf{K}_{33} = \int_\Omega \nabla\mathbf{N}^T\rho_{da}(K_a + HK_l)\nabla\mathbf{N}\,\mathrm{d}\Omega, \quad \mathbf{K}_{34} = \int_\Omega \nabla\mathbf{N}^T H\rho_{da} D_T \nabla\mathbf{N}\,\mathrm{d}\Omega,$$

$$\mathbf{K}_{42} = \int_\Omega \nabla\mathbf{N}^T D_{c2}^* \nabla\mathbf{N}\,\mathrm{d}\Omega, \quad \mathbf{K}_{43} = \int_\Omega \nabla\mathbf{N}^T D_{a2}^* \nabla\mathbf{N}\,\mathrm{d}\Omega, \quad \mathbf{K}_{44} = \int_\Omega \nabla\mathbf{N}^T D_{T2}^* \nabla\mathbf{N}\,\mathrm{d}\Omega,$$

$$\mathbf{F}_1 = \int_S \mathbf{N}^T\mathbf{t}\,\mathrm{d}S, \quad \mathbf{F}_2 = \int_S \mathbf{N}^T(\mathbf{q}_{vap} + \mathbf{q}_{liq})\cdot\mathrm{d}S - \int_\Omega \nabla\mathbf{N}^T\rho_l \mathrm{K}_l \nabla(\rho_l g z)\,\mathrm{d}\Omega$$

$$\mathbf{F}_3 = \int_S \mathbf{N}^T\mathbf{q}_{da}\cdot\mathrm{d}S - \int_\Omega \nabla\mathbf{N}^T H\rho_{da} K_l \nabla(\rho_l g z)\,\mathrm{d}\Omega,$$

$$\mathbf{F}_4 = \int_S \mathbf{N}^T\mathbf{q}_T\cdot\mathrm{d}S - \int_\Omega \nabla\mathbf{N}^T(C_l\rho_l + C_{da}\rho_{da}H)K_l T\nabla(\rho_l g z)\,\mathrm{d}\Omega,$$

$\mathbf{m} = \langle\ 1\ 1\ 0\ \rangle$ and $\mathbf{q}_{liq}$, $\mathbf{q}_{vap}$, $\mathbf{q}_{da}$ and $\mathbf{q}_T$ denote the specified liquid water, vapour water, dry air and heat fluxes at the boundary $\mathbf{S}$.

References

Biot, M.A., 1956. General solutions of the equations of elasticity and consolidation for a porous material. J. Appl. Mech. 23, 91–96.

Carnahan, C.L., 1984. Thermodynamic coupling of heat and matter flows in near-field regions of nuclear waste repositories. Proc. Mat. Res. Soc. Symp. 26, 1023–1030.

Carslaw, A.R., Jaegar, C.J., 1960. Conduction of Heat in Solids. Oxford at the Clarendon Press, London.

Fredlund, D.G., Hasan, J.U., 1979. One dimensional consolidation theory: unsaturated soils. Can. Geotech. J. 16, 521–531.

Fredlund, D.G., Rahardjo, E., 1993. Soil Mechanics for Unsaturated Soils. Wiley, New York.

Gillham, R.W., Klute, A., Heermann, D.F., 1979. Measurement and numerical simulation of hysteretic flow in a heterogeneous porous medium. Soil Sci. Soc. Amer. J. 40, 203–207.

Graham, J., Chandler, N.A., Dixon, D.A., Roach, P.J., To, T., Wan, A.W.L., 1996. The buffer/container experiment: vol. 4—results, synthesis, issues. Fuel Waste Technology, AECL, Whiteshell Laboratories, Pinawa.

Haverkamp, R., Vauclin, M., Touma, J., Wierenga, P.J., Vachaud, G., 1977. A comparison of numerical simulation models for one-dimensional infiltration. Soil Sci. Soc. Am. Proc. 41, 285–294.

Hillel, D., 1971. Soil and Water: Physical Principles and Processes. Academic Press, New York.

Horseman, S.T., McEwen, T.J., 1996. Thermal constraints on disposal of heat-emitting waste in argillaceous rocks. Eng. Geol. 41, 5–16.

Kay, B.D., Groenevelt, P.H., 1974. On the interaction of water and heat in frozen and unfrozen soils, 1. Basic theory: the vapour phase. Soil Sci. Soc. Am. Proc. 38, 395–400.

Kool, J.B., Parker, J.C., 1987. Development and evaluation of closed-form expressions for hysteretic soil hydraulic properties. Water Resour. Res. 23, 105–114.

Lewis, R.W., Schrefler, B.A., 1987. The Finite Element Method in the Deformation and Consolidation of Porous Media. Wiley, New York.

Lloret, A., Alonso, E.E., 1980. Consolidation of unsaturated soils including swelling and collapse behaviour. Geotechnique 30, 449–477.

Matyas, E.L. Radhakrisha, H.S. (1968). Volume change characteristic of partially saturated soils. Geotechnique 18, 432–448.

McTigue, D., 1990. Flow to a heated borehole in porous, thermoelastic rock: Analysis. Water Resour. Res. 26, 1763–1774.

Milly, P.C.D., 1982. Moisture and heat transport in hysteretic, inhomogeneous porous media: a matric head-based formulation and a numerical model. Water Resour. Res. 18, 489–498.

Milly, P.C.D., 1984. A simulation analysis of thermal effects on evaporation from soil. Water Resour. Res. 20, 1087–1098.

Milly, P.C.D., 1988. Advances in modelling of water in the unsaturated zone. Transport in Porous Media 3, 491–514.

Philip, J.R., 1957. The theory of infiltration, 1, The infiltration equation and its solution. Soil. Sci. 83, 345–357.

Philip, J.R., De Vries, D.A., 1957. Moisture movement in porous materials under temperature gradients. Trans. Am. Geophys. Union 38, 222–232.

Pickens, J.F., Gillham, R.W., 1980. Finite element analysis of solute transport under hysteretic unsaturated flow conditions. Water Resour. Res. 16, 1071–1078.

Rehbinder, G., 1995. Analytical solutions of stationary coupled thermo-hydro-mechanical problems. Int. J. Rock. Mech. Min. Sci. Geomech. Abstr. 32, 453–463.

Scott, P.S., Farquar, G.J., Kouwen, N., 1983. Hysteretic Effects on Net Infiltration. Advances in Infiltration. Am. Soc. Agric. Eng., St. Joseph, Michigan, pp. 163–170.

Srivastava, R.C., Avasthi, P.K., 1975. Non-equilibrium thermodynamics of thermo-osmosis of water through kaolinite. J. Hydrol. 24, 111–120.

Ten Berge, H.F.M., Bolt, G.H., 1988. Coupling between liquid flow and heat flow in porous media: a connection between two classical approaches. Transport in Porous Media 3, 35–49.

Thomas, H.R., He, Y., 1995. Analysis of coupled heat, moisture and air transfer in a deformable unsaturated soil. Geotechnique 45, 677–689.

Thomas, H.R., He, Y., Sansom, M.R., Li, C.L.W., 1996. On the development of a model of the thermo-mechanical-hydraulic behavior of unsaturated soils. Eng. Geol. 41, 197–218.

Villar, M.V., Martin, P.L., 1993. Suction controlled oedometric tests in mont-morillonite clay. Proceedings of the 29th Annual Conference of the Engineering Group of the Geological Society of London, pp. 337–342.

Villar, M.V., Cuevas, J., Fernandez, A.M., Martin, P.L., 1993. Effects of the interaction of heat and water flow in compacted bentonite. International Workshop on Thermomechanics of Clays and Clay Barriers, Bergamo.

Wheeler, S.J., Sivakumar, V., 1995. An elasto-plastic critical state framework for unsaturated soil. Geotechnique 45, 35–53.

Zhou, Y., Rajapakse, R.K.N.D., Graham, J., 1998. Coupled heat–moisture–air transfer in deformable unsaturated media. J. Eng. Mech. ASCE, 124, 1090–1099.

Zienkiewicz, O.C., Taylor, R.L., 1989. The Finite Element Method, 4th ed. McGraw–Hill, New York.